



Article

An Improved Physics-Based Dual-Band Model for Satellite-Derived Bathymetry Using SuperDove Imagery

Chunlong He, Qigang Jiang * and Peng Wang

College of Geoexploration Science and Technology, Jilin University, Changchun 130026, China; hecl22@mails.jlu.edu.cn (C.H.); pwang24@mails.jlu.edu.cn (P.W.)

* Correspondence: jiangqigang@jlu.edu.cn

Abstract: Shallow water bathymetry is critical for environmental monitoring and maritime security. Current widely used statistical models based on passive optical satellite remote sensing often rely on prior bathymetric data, limiting their application to regions lacking such information. In contrast, the physics-based dual-band log-linear analytical model (P-DLA) can estimate shallow water bathymetry without in situ measurements, offering significant potential. However, the quasi-analytical algorithm (QAA) used in the P-DLA is sensitive to non-ideal pixels, resulting in unstable bathymetry estimation. To address this issue and evaluate the potential of SuperDove imagery for bathymetry estimation in regions without prior bathymetric data, this study proposes an improved physics-based dual-band model (IPDB). The IPDB replaces the QAA with a spectral optimization algorithm that integrates deep and shallow water sample pixels to estimate diffuse attenuation coefficients for the blue and green bands. This allows for more accurate estimation of shallow water bathymetry. The IPDB was tested on SuperDove images of Dongdao Island, Yongxing Island, and Yongle Atoll. The results showed that SuperDove images are capable of estimating shallow water bathymetry in regions without prior bathymetric data. The IPDB achieved Root Mean Square Error (RMSE) values below 1.7 m and R^2 values above 0.89 in all three study areas, indicating strong performance in bathymetric estimation. Notably, the IPDB outperformed the standard P-DLA model in accuracy. Furthermore, this study outlines four sampling principles that, when followed, ensure that variations in the spatial distribution of sampling pixels do not significantly impact model performance. This study also showed that the blue–green band combination is optimal for the analytical expression of the physics-based dual-band model.

Keywords: remote sensing; dual band; spectral optimization algorithm; diffuse attenuation coefficients; water depth; bathymetric estimation



Citation: He, C.; Jiang, Q.; Wang, P. An Improved Physics-Based Dual-Band Model for Satellite-Derived Bathymetry Using SuperDove Imagery. *Remote Sens.* **2024**, *16*, 3801. <https://doi.org/10.3390/rs16203801>

Academic Editors: Jacek Lubczonek, Pawel Terefenko, Katarzyna Bradtke and Marta Włodarczyk-Sielicka

Received: 12 September 2024

Revised: 8 October 2024

Accepted: 11 October 2024

Published: 12 October 2024



Copyright: © 2024 by the authors. Licensee MDPI, Basel, Switzerland. This article is an open access article distributed under the terms and conditions of the Creative Commons Attribution (CC BY) license (<https://creativecommons.org/licenses/by/4.0/>).

1. Introduction

Shallow water bathymetry is a critical parameter for various marine applications, including maritime navigation, coastal management, underwater habitat mapping, and coral reef conservation [1–3]. While ship-based single/multibeam sonar and airborne LiDAR systems offer high measurement accuracy, these traditional methods are costly and limited in coverage. In shallow waters, the navigation capabilities of survey vessels are often restricted [4–6]. In contrast, satellite-derived bathymetry (SDB) presents a cost-effective alternative with extensive coverage and temporal flexibility, making it particularly valuable as a supplement to traditional methods in shallow and remote areas [7–10].

Over the past few decades, numerous satellite bathymetry algorithms have been developed, leveraging optical satellite remote sensing data. These algorithms can be broadly classified into statistical models and semi-analytical models. Statistical models, including log-linear models, log-ratio models, and machine learning approaches, are well established but rely on prior bathymetric data (such as in situ measurements), limiting their scalability to other regions [11–15]. With the launch of the ICESat-2 satellite, many studies

have adopted statistical models for active–passive fusion bathymetry, as ICESat-2 data can replace in situ bathymetry for accurate depth estimation [16–21]. However, ICESat-2's trajectory may not cover some shallow areas, such as small islands and coastal locations, preventing the construction of statistical models in these regions without prior bathymetric data [22]. Semi-analytical models, on the other hand, are based on radiative transfer theory for optically shallow waters, allowing for depth estimation without the need for prior bathymetry. A variety of semi-analytical models have been developed, including HOPE, M-HOPE, UMOPE, and L-S algorithms [23–28].

The HOPE algorithm was initially designed for hyperspectral imagery, which provides enough spectral bands to avoid ill-posed spectral optimization equations. However, it often generates false estimation in low-reflectance waters and is computationally inefficient due to its pixel-by-pixel iterative mechanism [26,28,29]. In tropical island regions with frequent cloud cover, suitable hyperspectral imagery is difficult to acquire and often lacks high spatial resolution. In contrast, multispectral imagery, which is more readily available and offers higher spatial resolution, is preferred for bathymetry in regions with frequent cloud cover [30,31]. To prevent the failure of semi-analytical models due to the limited spectral bands of multispectral images, the HOPE algorithm needs to be simplified, reducing the number of unknowns to enable depth estimation from images with fewer bands [32–34]. If water clarity is uniform across the area, the optimal inherent optical properties (IOPs) of the water column can be calculated using remote sensing reflectance from adjacent optically deep waters, treating the three unknowns in the HOPE algorithm as constants. However, even in high-resolution multispectral imagery, pixel-by-pixel spectral optimization remains time-consuming. Assuming a positive correlation between depths estimated by statistical and semi-analytical models, optimal IOPs can be determined by iterating through all possible IOP combinations. However, false correlations between depths may result in larger estimation errors.

Chen proposed a physics-based dual-band log-linear analytical model (P-DLA) in which all unknowns can be directly estimated from different types of sample pixels in remote sensing imagery [35–37]. The P-DLA model's advantage is that it can accurately estimate depths without prior bathymetric data or pixel-by-pixel spectral optimization. While theoretically applicable to most high-resolution remote sensing images, the P-DLA model has been underexplored in practice and presents certain limitations. One key limitation is that in the P-DLA model, the empirical estimation of the green band absorption coefficient from neighboring optically deep waters can be influenced by non-ideal pixels. This reduces the accuracy of the quasi-analytical algorithm (QAA) in estimating the diffuse attenuation coefficient for the green band, ultimately lowering the accuracy of bathymetric estimation accuracy. To overcome this issue, we propose a spectral optimization algorithm (SOA), which integrates sampling pixels from both optically deep and shallow waters to estimate the diffuse attenuation coefficients for the blue and green bands. The SOA incorporates spectral models for the absorption coefficients of phytoplankton and colored dissolved organic matter (CDOM), resulting in more accurate attenuation coefficient estimations. Based on this improvement, we develop an improved physics-based dual-band model (IPDB) for shallow water bathymetry estimation. Additionally, we evaluate the effectiveness of the IPDB model using SuperDove imagery. Compared to commonly used Sentinel-2 and Landsat-8/9 images, SuperDove offers a shorter revisit time and higher spatial resolution, making it especially valuable in tropical island regions where frequent cloud cover is an issue.

The key innovation of this study lies in evaluating the potential of SuperDove imagery for shallow water bathymetry estimation in the absence of prior bathymetric data and developing an improved version of the P-DLA model, the IPDB.

2. Study Area and Data

2.1. Study Area

The study area is located in the Xisha Islands of the South China Sea, specifically around Dongdao Island, Yongxing Island, and the northern part of Yongle Atoll (referred to simply as Yongle Atoll for brevity), as shown in Figure 1. These islands and reefs feature a mixed sandy and coral reef substrate and are relatively well preserved in their natural state, with minimal human impact. The region experiences a tropical marine climate, and the surrounding waters are clear, making it an ideal area for remote sensing-based shallow water bathymetry studies.

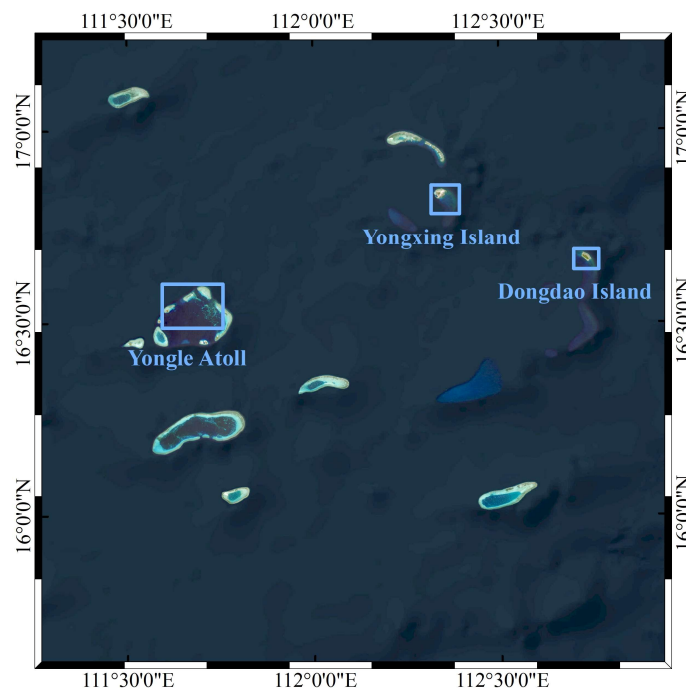


Figure 1. Geographic distribution of the study area.

2.2. Data

The in situ bathymetric data used in this study were obtained from the national foundational research project “Survey of Coral Reefs in the Central and Northern South China Sea” (Project Number: 2012FY112400), which is fully available at the National Earth System Science Data Center (<https://www.geodata.cn>, accessed on 3 July 2024). The project team conducted transect-based continuous depth measurements in the field, with navigation using a Hi-Target beacon K3DGPS, achieving a positioning accuracy better than 10 m. Depth measurements were performed using a Hi-Target high-frequency echosounder HD370, with an accuracy better than 0.3 m. The in situ bathymetric data consist of single-beam measurements represented as individual points with corresponding latitude and longitude coordinates, water depth values, and acquisition times. The bathymetry values from the in situ bathymetric data are instantaneous bathymetry values, which subsequently require tide correction using tidal data, i.e., the bathymetry values from the in situ bathymetric data are first calibrated to the theoretical lowest tidal level, and then to the instantaneous bathymetry values at the time of imaging. The collection dates for the in situ bathymetric data are shown in Figure 2 and Table 1. The number of measured depth points in Dongdao Island, Yongxing Island, and Yongle Atoll were 2633, 2198, and 2941, respectively. The spatial distribution of these points is illustrated in Figure 2.

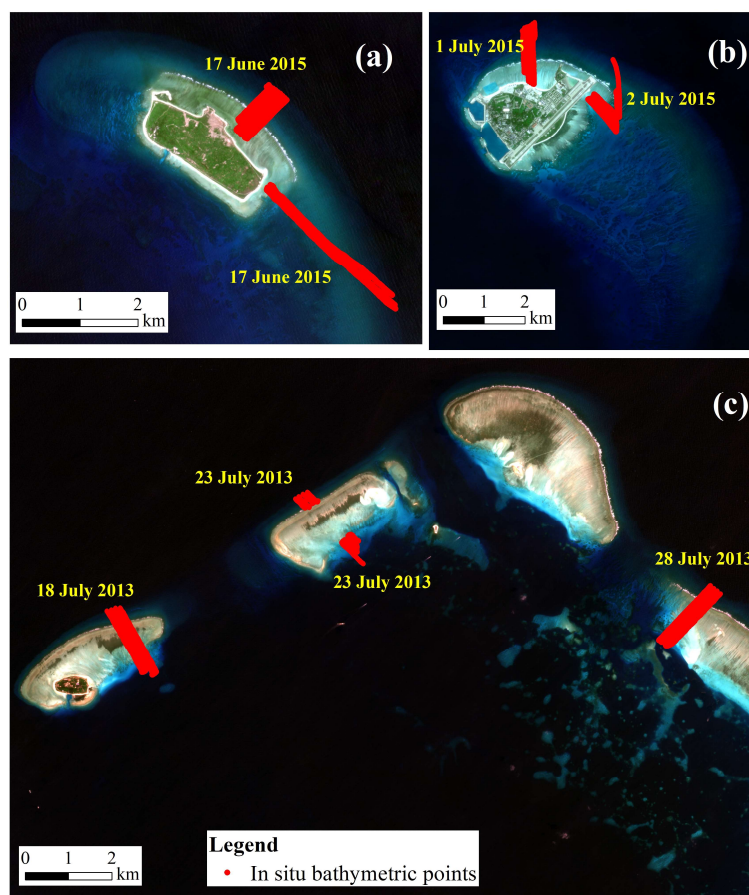


Figure 2. Spatial distribution of measured bathymetric data. (a) Dongdao Island; (b) Yongxing Island; (c) Yongle Atoll. The yellow text in the figures indicates the collection dates of the nearest bathymetric lines.

Table 1. Data acquisition date.

Data Type	Study Area	Acquisition Date
Bathymetric data	Dongdao Island	17 June 2015
	Yongxing Island	1 July 2015
		2 July 2015
	Yongle Atoll	23 July 2013
18 July 2013		
28 July 2013		
Remote sensing imagery	Dongdao Island	29 August 2021
	Yongxing Island	4 November 2022
	Yongle Atoll	2 March 2022

The remote sensing imagery was provided by Planet Labs (www.planet.com/account, accessed on 28 June 2024) in the form of PlanetScope SuperDove Level 3B surface reflectance data products (referred to as SuperDove). These data have undergone sensor calibration, radiometric correction (referenced to Sentinel-2 imagery), and orthorectification. Additional atmospheric corrections have been applied using the 6S radiative transfer model and near real-time MODIS data. SuperDove images have a spatial resolution of 3 m and a revisit period of 1–2 days. The images have eight spectral bands, including coastal blue (441.5 nm), blue (490 nm), green I (531 nm), green (565 nm), yellow (610 nm), red (665 nm), red edge (705 nm), and near-infrared (865 nm). The acquisition dates for the remote sensing data are provided in Table 1.

3. Methodology

The workflow for satellite-derived bathymetry (SDB) is shown in Figure 3. It begins with data preprocessing, which includes preparing remote sensing images (cloud mask, sea–land segmentation, white wave mask, and sun glint correction) and field depth data (tide correction). Next, shallow water depths are estimated using the physics-based dual-band log-linear analytical model (P-DLA) and the improved physics-based dual-band model (IPDB). Postprocessing is then applied to the depth estimation from both models, which includes median filtering and masking deep water areas. Finally, the accuracy of the satellite-derived bathymetry is evaluated.

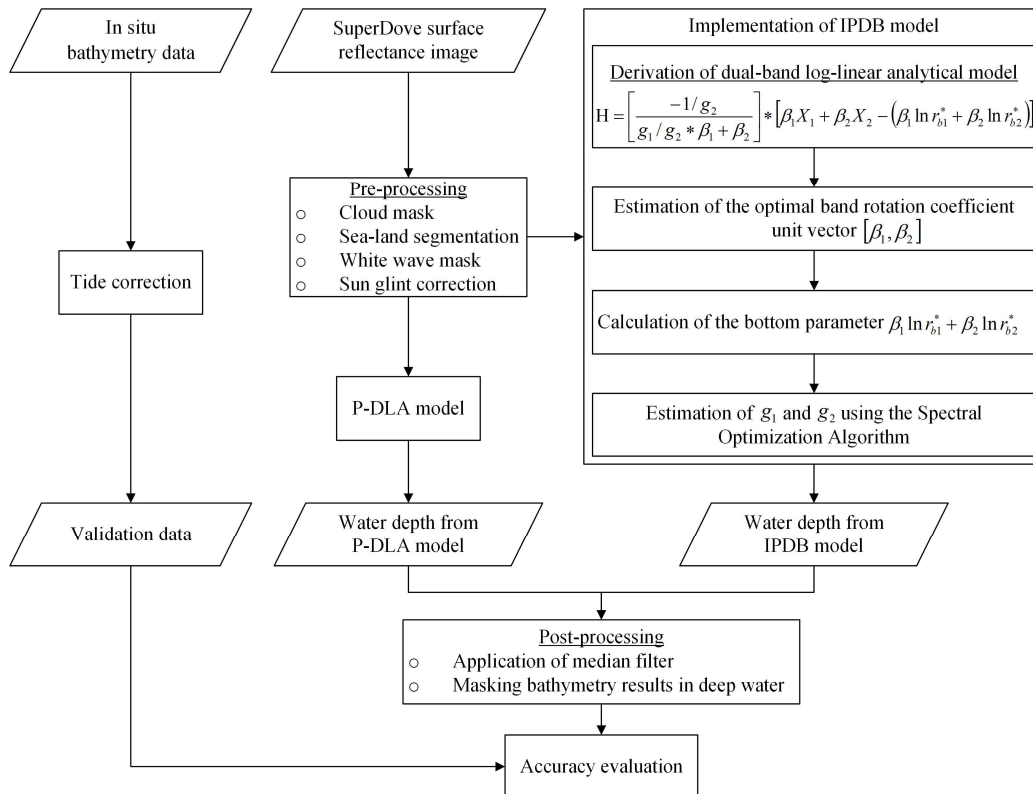


Figure 3. Technical workflow for satellite-derived bathymetry.

3.1. Data Preprocessing

Field depth measurements represent instantaneous data collected at a single time point and are not corrected for tidal variation. Additionally, the time of depth measurement does not coincide with the acquisition time of the multispectral images. To resolve this, we apply Equation (1) to calibrate the field depths to the corresponding depths at the imaging time using tidal data from the Dayu Tidal Table (www.chaoxibiao.net, accessed on 30 July 2024). Tidal heights at both the field measurement time and imaging time are interpolated using a cubic spline function.

$$H(t_2) = H(t_1) - \Delta H(t_1) + \Delta H(t_2) \quad (1)$$

where t_1 is the field measurement time, and t_2 is the imaging time of the multispectral image. $H(t_1)$ and $H(t_2)$ represent the instantaneous field depth and the imaging depth, respectively. $\Delta H(t_1)$ and $\Delta H(t_2)$ are the tidal heights at the field measurement and imaging times, respectively. After tide correction, the field bathymetric points are used as the validation set for model accuracy assessment, and the maximum depth recorded in each of the three study areas is 25 m.

Preprocessing of the remote sensing images involves cloud mask, sea–land segmentation, white wave mask, and sun glint correction. Cloud cover, which affects the retrieval of

surface information, is manually masked by visual interpretation. Sea–land segmentation is performed to reduce data volume and computation time by defining ocean areas as those with near-infrared (NIR) reflectance below 0.2. A white wave mask is manually generated to avoid noise in depth measurements caused by white waves. In clear waters, sun glint can interfere with visible wavelengths, obscuring underwater features. If necessary, Hedley’s method is used to correct for sun glint, as shown in Equation (2) [38].

$$\rho_m = \rho_\lambda - b_\lambda (\rho_{NIR} - \rho_{NIR}^{min}) \quad (2)$$

where ρ_m is the surface reflectance after sun glint correction, ρ_λ is the original surface reflectance, ρ_{NIR} is the NIR band reflectance, ρ_{NIR}^{min} is the minimum reflectance within the given region, and b_λ is the regression slope between the visible band reflectance and NIR reflectance. In this study, sun glint correction was applied only to the SuperDove imagery from Yongle Atoll.

3.2. Implementation of the Improved Physics-Based Dual-Band Model

3.2.1. Derivation of the Physics-Based Dual-Band Log-Linear Analytical Model

Using the surface reflectance ρ_m , the remote sensing reflectance R_{rs} is calculated as $R_{rs} = \rho_m / \pi$. The subsurface remote sensing reflectance r_{rs} can then be derived using Equation (3).

$$r_{rs} = \frac{R_{rs}}{0.52 + 1.7R_{rs}} \quad (3)$$

Assuming a Lambertian bottom, the subsurface reflectance r_{rs} in optically shallow waters can be expressed as a function of the deep water subsurface reflectance r_{rs}^{dp} , the downwelling diffuse attenuation coefficient k_d , the upwelling radiance attenuation coefficients for water column scattering k_c , the upwelling radiance attenuation coefficients for bottom reflection k_b , the bottom albedo ρ_b , and the water depth H , as shown in Equation (4) (wavelength λ omitted for simplicity) [25].

$$r_{rs} = r_{rs}^{dp} \{1 - \exp[-(k_d + k_c)H]\} + \frac{\rho_b}{\pi} \exp[-(k_d + k_b)H] \quad (4)$$

For simplicity, it is often assumed that $k_c = k_b$, and a single attenuation coefficient k is used to replace them, simplifying Equations (4) and (5).

$$r_{rs} = r_{rs}^{dp} [1 - \exp(-gH)] + r_b \exp(-gH) \quad (5)$$

where $g = k_d + k$ is the sum of the downwelling and upwelling diffuse attenuation coefficients, and $r_b = \rho_b / \pi$. Taking the natural logarithm of both sides leads to the single-band log-linear model, as shown in Equation (6).

$$X = -gH + \ln r_b^* \quad (6)$$

where $X = \ln(r_{rs} - r_{rs}^{dp})$, and $\ln r_b^* = \ln(r_b - r_{rs}^{dp})$, typically used for natural waters. The dual-band log-linear model, using blue and green bands, can be expressed as a more general vector equation, shown in Equation (7) [35,39].

$$\vec{\alpha} \cdot \vec{X} = \vec{\alpha} \cdot \ln \vec{r}_b - (\vec{\alpha} \cdot \vec{g})H \quad (7)$$

where $\vec{X} = [X_1, X_2]$, $\ln \vec{r}_b = [\ln r_{b1}^*, \ln r_{b2}^*]$, $\vec{g} = [g_1, g_2]$, and $\vec{\alpha} = [\alpha_1, \alpha_2]$ represents the arbitrary band rotation coefficient unit vector for the blue and green bands. The optimal band rotation coefficient unit vector, represented by $\vec{\beta} (= [\beta_1, \beta_2])$, is a special case of $\vec{\alpha}$,

minimizing the influence of the bottom type on depth estimation. When $\vec{\alpha} = \vec{\beta}$, the dual-band log-linear model becomes the analytical solution shown in Equation (8).

$$H = \left[\frac{-1/g_2}{g_1/g_2 * \beta_1 + \beta_2} \right] * [\beta_1 X_1 + \beta_2 X_2 - (\beta_1 \ln r_{b1}^* + \beta_2 \ln r_{b2}^*)] \quad (8)$$

The dual-band log-linear analytical model, as expressed in Equation (8), provides a clear framework for estimating shallow water depth. In a two-dimensional coordinate space, data from different substrate types, represented by X_1 and X_2 , are linearly transformed by the vector $\vec{\beta}$. This transformation isolates a new variable, $Y (= \beta_1 X_1 + \beta_2 X_2)$, which is highly correlated with water depth and largely independent of substrate variation. In this framework, the values $\beta_1 \ln r_{b1}^* + \beta_2 \ln r_{b2}^*$ correspond to the Y value at zero depth, or the waterline. To adjust Y to reflect the water depth H , the parameter factor $\frac{-1/g_2}{g_1/g_2 * \beta_1 + \beta_2}$ is applied. By estimating these parameters from remote sensing images, it is possible to accurately determine shallow water depth.

3.2.2. Estimation of the Optimal Band Rotation Coefficient Unit Vector $\vec{\beta}$

For shallow waters with varying substrate types, the optimal band rotation coefficient unit vector $\vec{\beta}$ should ensure that the variable Y not only has the strongest correlation with water depth but is also minimally affected by changes in substrate type. Assuming that the seafloor topography does not change abruptly and that the spatial resolution of the remote sensing image is sufficiently high, the water depth of two adjacent pixels parallel to the waterline can be assumed to be approximately equal [35]. Based on this assumption, a set of adjacent pixel pairs, represented as the dataset $X_1 \sim X_2$, can be randomly and uniformly selected from high-resolution remote sensing images to estimate $\vec{\beta}$. These pixel pairs should differ in their distance from the waterline and be located at the boundary between different substrate types. When $\vec{\beta}$ is applied to the $X_1 \sim X_2$ dataset, the Y values for pixel pairs with the same depth should be equal or as close as possible.

For each adjacent pixel pair, the difference in the Y value pairs (Y_A and Y_B) corresponding to $\vec{\beta}$ is calculated, referred to as ΔSH_i , as shown in Equations (9)–(11).

$$\Delta SH_i = |Y_A - Y_B|_i \quad (9)$$

$$\Delta SH_i = \left| (\beta_1 X_1^A + \beta_2 X_2^A) - (\beta_1 X_1^B + \beta_2 X_2^B) \right|_i \quad (10)$$

$$\Delta SH_i = \left| \beta_1 (X_1^A - X_1^B) + \beta_2 (X_2^A - X_2^B) \right|_i \quad (11)$$

where i denotes a specific adjacent pixel pair, and A and B represent two different substrate types in the pair.

According to the previous assumption, adjacent pixel pairs have similar water depths. Thus, in theory, the difference between any Y value pairs corresponding to $\vec{\beta}$ should be zero, and the sum of all such differences should also be zero. However, due to inherent variability in water properties and bottom reflectance across spatial locations, $\vec{\beta}$ cannot guarantee that the sum of Y value differences is exactly zero. Therefore, $\vec{\beta}$ is determined by minimizing the function shown in Equation (12).

$$f(\beta_1, \beta_2) = \operatorname{argmin} \left[\sum_{i=1}^n (\Delta SH_i)^2 \right] \quad (12)$$

where n represents the number of adjacent pixel pairs, and $\left| \vec{\beta} \right| = 1$.

3.2.3. Calculation of the Bottom Parameter $\beta_1 \ln r_{b1}^* + \beta_2 \ln r_{b2}^*$

According to Equation (8), when the water depth is zero, $\beta_1 \ln r_{b1}^* + \beta_2 \ln r_{b2}^*$ is equal to $\beta_1 X_1 + \beta_2 X_2$. Theoretically, the values of $\beta_1 \ln r_{b1}^* + \beta_2 \ln r_{b2}^*$ should be the same for different substrate types. However, in real water environments, slight variations in these values may occur due to differences in bottom reflectance that cannot be completely eliminated. In practice, efforts should be made to account for various bottom reflectance types in the calculations.

Near the waterline, where the water depth can be assumed to be zero, several substrate types (e.g., sand, coral reefs, algae, and other less distinguishable bottom substrates) are usually present and consistent with those in the shallow water region. Based on this, a set of sampling pixels representing different substrate types near the waterline can be selected. The values of $\beta_1 X_1 + \beta_2 X_2$ for these pixels can then be calculated as the values of $\beta_1 \ln r_{b1}^* + \beta_2 \ln r_{b2}^*$. The average of these values for various substrate types is used to estimate the bottom parameters for the study area.

3.2.4. Estimation of g_1 and g_2 Using the Spectral Optimization Algorithm (SOA)

By applying Equation (5) to the blue and green bands and eliminating the water depth variable H , Equations (13) and (14) are obtained.

In optical shallow water, the following hold:

$$X_1 = (g_1/g_2) * X_2 + M \quad (13)$$

$$M = \ln r_{b1}^* - (g_1/g_2) * \ln r_{b2}^* \quad (14)$$

Here, M varies with different substrate types and can be used as a characteristic indicator of the substrate. Assuming uniform water properties in the study area, the ratio of blue to green band diffuse attenuation coefficients (g_1/g_2) remains constant across the area. As shown in Equation (13), the slope of the regression equation constructed from the $X_1 \sim X_2$ dataset for the same substrate type (e.g., sand) but at different depths should be approximately equal to g_1/g_2 , provided the coefficient of determination R^2 is close to 1 (typically $R^2 > 0.9$). After estimating g_1/g_2 , the green band diffuse attenuation coefficient g_2 remains unknown.

In the study area, the inherent optical properties of the water typically show little variability and can be treated as approximate constants [27,32]. Generally, the diffuse attenuation coefficient estimated from the deep water region is applicable to the entire shallow region [24]. However, in the P-DLA model, estimating the green band absorption coefficient in optically deep water without considering the spectral model of phytoplankton and colored dissolved organic matter absorption can cause instability in the QAA's estimated g_2 , thereby affecting the accuracy of the water depth estimation.

To address the above limitations, this study introduces an improved P-DLA model that uses a spectral optimization algorithm (SOA) to estimate the diffuse attenuation coefficients for the blue and green bands. Unlike the P-DLA model, where the g_1/g_2 ratio derived from optically shallow water is applied directly to the model coefficients, the IPDB model uses this ratio as a constraint within the SOA. This is because sampling from both optically deep and shallow water generally provides more stable estimation of the diffuse attenuation coefficients. The SOA used in this study is outlined below, with the wavelength λ omitted for simplicity.

In optical deep water, the following hold [26,35,40]:

$$a_{phy} = [a_0 + a_1 \ln P]P \quad (15)$$

$$a_{dg} = G * \exp(-0.014 * (\lambda - 440)) \quad (16)$$

$$a = a_w + a_{phy} + a_{dg} \quad (17)$$

$$b_{bw} = 0.00144 \left(\frac{\lambda}{500} \right)^{-4.32} \quad (18)$$

$$b_{bp} = X \left(\frac{400}{\lambda} \right)^{0.681} \quad (19)$$

$$b_b = b_{bw} + b_{bp} \quad (20)$$

$$u_m = \frac{b_b}{a + b_b} \quad (21)$$

$$kd = (1 + m_0 * \theta_s) a + \left(1 - \gamma \frac{b_{bw}}{b_b} \right) * m_1 * (1 - m_2 * e^{-m_3 * a}) b_b \quad (22)$$

$$k_u^C = \frac{1}{\cos(\theta_v)} (a + b_b) * D_u^C \quad (23)$$

$$D_u^C = 1.03(1 + 2.4u_m)^{0.5} \quad (24)$$

$$k_u^B = \frac{1}{\cos(\theta_v)} (a + b_b) * D_u^B \quad (25)$$

$$D_u^B = 1.04(1 + 5.4u_m)^{0.5} \quad (26)$$

$$g_m = kd + (k_u^C + k_u^B) / 2 \quad (27)$$

In this case, u_m is the inherent optical parameter, and g_m is the diffuse attenuation coefficient. The absorption coefficient of water is denoted as a , where a_w is the absorption coefficient of pure water, a_{phy} is the absorption coefficient of phytoplankton, and a_{dg} is the absorption coefficient of colored dissolved organic matter (yellow substances). The backscattering coefficient b_b consists of the pure water backscattering coefficient b_{bw} and the suspended particle backscattering coefficient b_{bp} . P is the absorption coefficient of phytoplankton at 440 nm, G is the absorption coefficient of yellow substances at 440 nm, and X is the backscattering coefficient of suspended particles at 400 nm. The empirical coefficients a_0 and a_1 are given in reference [41]. The variables θ_s and θ_v are the subsurface solar zenith angle and the subsurface satellite viewing angle, respectively. The constants m_{0-3} and γ , which are independent of water properties and spectral wavelength, have fixed values of 0.005, 4.26, 0.52, 10.8, and 0.265.

Thus, in optical deep water, u_m and g_m can be expressed as functions of the unknowns P , G , and X :

$$u_m(\lambda) = f_1(P, G, X, \lambda) \quad (28)$$

$$g_m(\lambda) = f_2(P, G, X, \lambda) \quad (29)$$

The inherent optical properties and attenuation coefficients for specific bands are then approximated using the sensor's spectral response function:

$$u_m(Band_i) \approx \frac{\int_{\lambda_{lower}}^{\lambda_{upper}} u_m(\lambda) RSR_i(\lambda) d\lambda}{\int_{\lambda_{lower}}^{\lambda_{upper}} RSR_i(\lambda) d\lambda} \quad (30)$$

$$g_m(Band_i) \approx \frac{\int_{\lambda_{lower}}^{\lambda_{upper}} g_m(\lambda) RSR_i(\lambda) d\lambda}{\int_{\lambda_{lower}}^{\lambda_{upper}} RSR_i(\lambda) d\lambda} \quad (31)$$

Here, $Band_i$ refers to the sensor band, and $RSR_i(\lambda)$ is the spectral response function of the band.

In the optical deep water region, the QAA is used to estimate the inherent optical parameters for the sensor's bands, as shown in Equation (32) [42,43].

$$u = \frac{-p_0 + \left[p_0^2 + 4p_1 * r_{rs}^{dp} \right]^{0.5}}{2p_1} \quad (32)$$

Here, p_0 and p_1 are model constants, with values of 0.0895 and 0.1247, respectively. The variable r_{rs}^{dp} represents the subsurface remote sensing reflectance for the optical deep water region and can be calculated using Equation (3).

In the optical deep water region, the difference between the simulated inherent optical parameter (u_m) and the actual inherent optical parameter (u) for specific bands should theoretically be minimized. Even when using sampling pixels solely from the deep water region, we can still estimate the diffuse attenuation coefficients for the blue and green bands based on the spectral optimization algorithm. The estimation is achieved by minimizing the following objective function:

$$obj_1 = \frac{\sqrt{\sum_{i=1}^3 (u_i^{mod} - u_i)^2}}{\sum_{i=1}^3 u_i} \quad (33)$$

Here, the subscripts 1, 2, and 3 refer to the blue, green, and red bands of the sensor, respectively. In the adjacent optical deep water, u_i^{mod} represents the simulated result from Equation (30), while u_i is the calculated result from Equation (32). The unknowns P , G , and X are estimated by minimizing the objective function. The minimization process is performed using the Trust Region Reflective algorithm from the SciPy library in Python, with the initial values and ranges for P , G , and X based on reference [25]. Once P , G , and X are determined, the blue band diffuse attenuation coefficient g_1 and the green band diffuse attenuation coefficient g_2 are calculated using Equation (31).

Adding appropriate constraints in the spectral optimization algorithm can often lead to more accurate results. In the optical shallow water region, the ratio of blue to green band diffuse attenuation coefficients, $M_k \approx g_1/g_2$, is estimated based on sandy pixel samples at different depths. Meanwhile, in the optical deep water region, the diffuse attenuation coefficients g_1^{mod} for the blue band and g_2^{mod} for the green band are simulated based on deep water samples. Theoretically, the ratio g_1^{mod}/g_2^{mod} in the deep water region should be as close as possible to the ratio M_k estimated in the shallow water region. By combining sample pixels in deep water and sandy sample pixels at different depths in shallow water, the spectral optimization algorithm can more accurately estimate the diffuse attenuation coefficients for the blue and green bands. This is achieved by minimizing the following objective function:

$$obj_2 = \frac{\sqrt{\sum_{i=1}^3 (u_i^{mod} - u_i)^2}}{\sum_{i=1}^3 u_i} + \frac{\sqrt{(g_1^{mod}/g_2^{mod} - M_k)^2}}{M_k} \quad (34)$$

Again, subscripts 1, 2, and 3 correspond to the blue, green, and red bands of the sensor. In adjacent optical deep waters, u_i^{mod} is the simulated result from Equation (30), while u_i is the calculated result from Equation (32). The parameters g_1^{mod} and g_2^{mod} are derived from Equation (31), and M_k is the slope of the regression equation constructed in the optical shallow water region, where $M_k \approx g_1/g_2$. The unknowns P , G , and X are estimated by minimizing the objective function using the Trust Region Reflective algorithm from the SciPy library, with initial values and parameter ranges based on reference [25]. Once P , G , and X are determined, the diffuse attenuation coefficients g_1 for the blue band and g_2 for the green band are calculated using Equation (31).

3.3. Application of Median Filter and Masking of Deep Water Results

After estimating g_1 and g_2 , the coefficients of the IPDB model are determined, allowing for the estimation of water depth across the entire area from the SuperDove imagery. To reduce speckle noise in the water depth estimation results, a two-dimensional median filter with a kernel size of 3 is applied. Optical remote sensing bathymetry is only valid in shallow waters, as “pseudo-shallow” distortions can occur in deep water regions. Therefore, it is necessary to mask out the results from the deep water regions.

In this study, a random forest classifier is used to identify deep water regions due to its robust performance and insensitivity to parameter variations. The classifier is sourced from ENMAP-BOX v2.1.1 and integrated into ENVI v5.6 as a plugin, retaining the default parameters [44]. Training samples for the classifier are visually selected from the preprocessed SuperDove imagery according to the principles of representativeness, full coverage and uniform distribution, with a separability index greater than 1.9. Shallow water samples are selected from regions where the water depth is less than 25 m, excluding “pseudo-shallow” areas, while deep water samples are taken from regions where the estimated depth exceeds 25 m, including some “pseudo-shallow” areas.

Although treating areas with depths greater than 25 m as optical deep water may not be strictly accurate, this assumption does not affect the core findings of this study, and its impact on the final conclusions is negligible.

3.4. Accuracy Evaluation Metrics

In this study, the accuracy of satellite-derived bathymetry is evaluated using the root mean square error (RMSE) and the coefficient of determination (R^2). RMSE measures the discrepancy between the estimated and measured water depths, with lower RMSE values indicating more accurate depth estimation. The R^2 value indicates the goodness of fit between the estimated and measured depths, ranging from 0 to 1. A value closer to 1 reflects better performance of the satellite-derived bathymetry.

$$\text{RMSE} = \sqrt{\frac{\sum_{i=1}^n (y_i - y_i^T)^2}{n}} \quad (35)$$

$$R^2 = \frac{\sum_{i=1}^n (y_i - \bar{y})^2}{\sum_{i=1}^n (y_i^T - \bar{y})^2} \quad (36)$$

where y_i and y_i^T represent the estimated and measured water depths for the i th validation sample, \bar{y} is the mean of the measured water depths, and n is the total number of validation samples.

4. Results

4.1. Model Parameter Estimation

For each of the three study areas, four types of pixel samples were collected from the preprocessed SuperDove imagery. These included adjacent pixel pairs of different depths at the boundaries of different substrate types, pixels of the same substrate type (e.g., sandy) but different depths, pixels of typical substrate types near the waterline (on the water side), and pixels of optically deep water adjacent to optically shallow water. The spatial distribution of these sample pixels is shown in Figure 4.

Regression equations were constructed based on the $X_1 \sim X_2$ datasets of sandy pixel samples at different depths for Dongdao Island, Yongxing Island, and Yongle Atoll. The slopes of these equations are shown in Figure 5a–c. The R^2 values of the fitted equations in all three areas exceed 0.9, with approximate g_1/g_2 ratios of 0.399, 0.523, and 0.525 for Dongdao, Yongxing, and Yongle, respectively. These g_1/g_2 ratios were used as constraints in the spectral optimization algorithm (SOA).

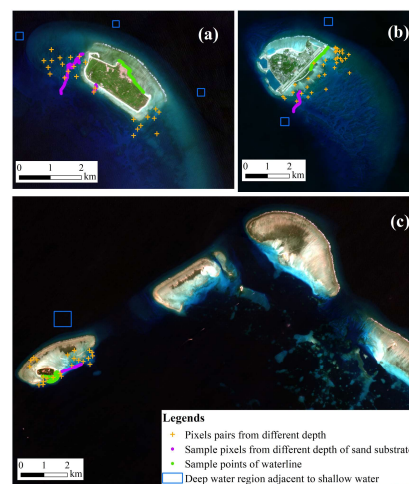


Figure 4. Distribution of sample pixels: (a) Dongdao Island; (b) Yongxing Island; (c) Yongle Atoll.

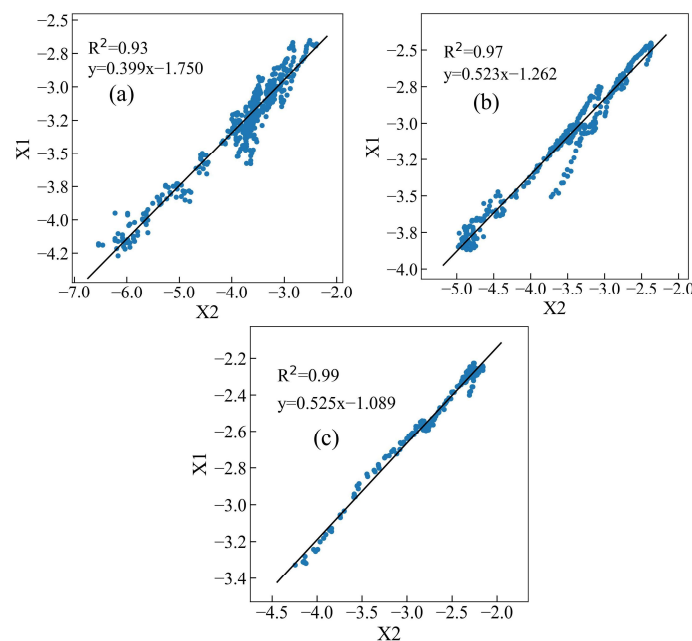


Figure 5. Estimated g_1/g_2 ratios from the $X_1 \sim X_2$ datasets for the same substrate type but different depths: (a) Dongdao Island; (b) Yongxing Island; (c) Yongle Atoll.

Based on the sample pixels, the required parameters for the IPDB model in each study area were estimated. These included the optimal band rotation coefficient unit vector $[\beta_1, \beta_2]$, the substrate parameter $\beta_1 \ln r_{b1}^* + \beta_2 \ln r_{b2}^*$, the diffuse attenuation coefficient for the blue band (g_1), and the diffuse attenuation coefficient for the green band (g_2). Applying these parameters to Equation (8) allowed for the estimation of shallow water depths in the study areas. The estimated model parameters are shown in Table 2.

Table 2. Model parameter estimation results.

Study Area	β_1	β_2	$\beta_1 \ln r_{b1}^* + \beta_2 \ln r_{b2}^*$	g_1	g_2
Dongdao Island	−0.457	0.890	−0.805	0.074	0.167
Yongxing Island	−0.580	0.815	−0.358	0.092	0.173
Yongle Atoll	−0.513	0.858	−0.651	0.090	0.171

4.2. Bathymetry Estimation

The IPDB model was applied to the preprocessed SuperDove imagery for all three study areas to estimate bathymetry. The final depth estimation results are shown in Figure 6. In the figure, gray areas represent land, cloud cover, or regions with white waves, while black areas indicate deep water regions. The estimated water depths range from 0 to 25 m. From Figure 6a–c, the detailed topographical features of the reefs and underwater formations are clearly visible. All three areas exhibit a consistent trend of “shallow water to deep water” from the reefs outward, demonstrating that SuperDove imagery is capable of estimating shallow water bathymetry without prior depth data.

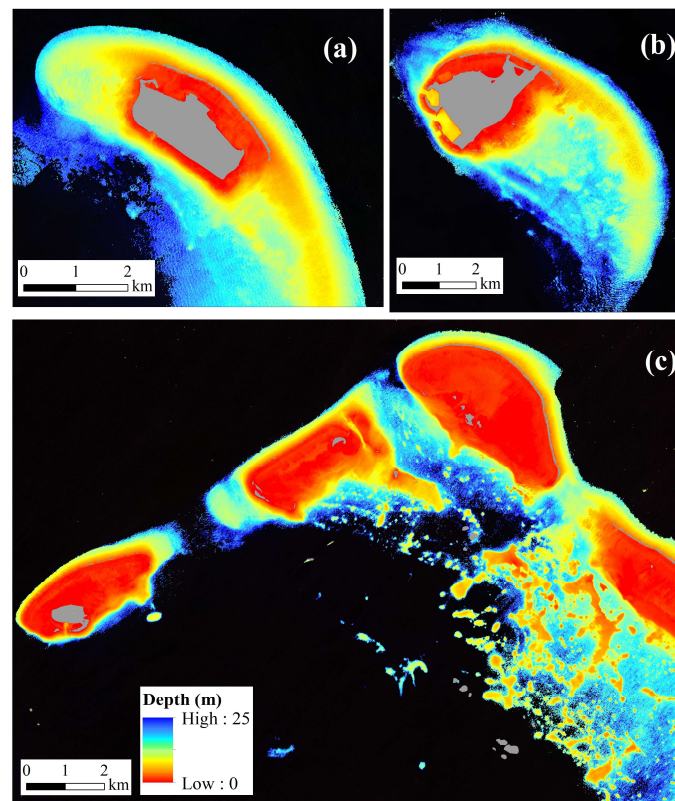


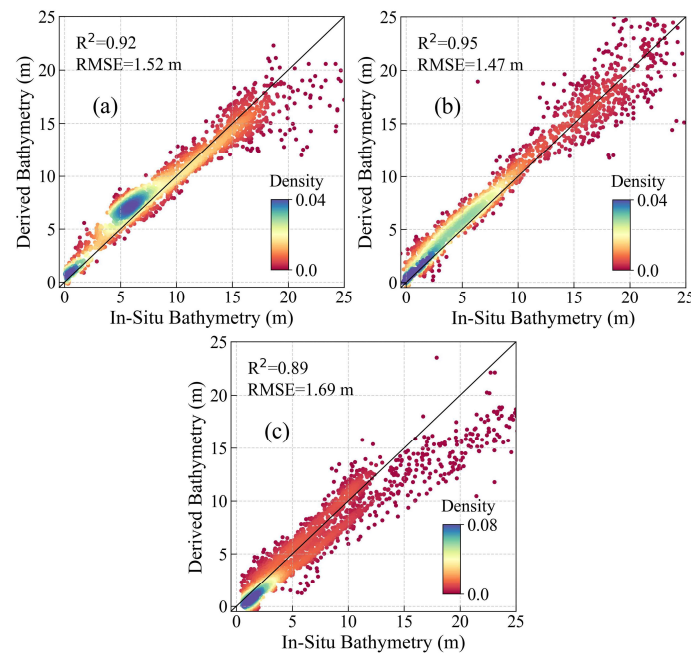
Figure 6. Bathymetry maps derived from the IPDB model: (a) Dongdao Island; (b) Yongxing Island; (c) Yongle Atoll.

4.3. Accuracy Evaluation

To evaluate the accuracy of the IPDB model, bathymetry estimation results for the three study areas were compared against validation datasets. The accuracy metrics are summarized in Table 3. The RMSE values for all three areas are less than 1.7 m, and the R^2 values exceed 0.89, with an average RMSE of 1.560 m and an average R^2 of 0.920. These results indicate high accuracy of the IPDB model across the study areas. Figure 7 shows scatter plots for each area, with data points closely aligned with the 1:1 line, further validating the accuracy of the depth estimation. Additionally, the scatter plots reveal that most data points for depths between 0 and 15 m are tightly clustered around the 1:1 line. However, as the depth exceeds 15 m, the scatter begins to diverge. Overall, the IPDB model demonstrates satisfactory performance in estimating bathymetry using SuperDove imagery.

Table 3. Accuracy evaluation results of the IPDB model.

Study Area	RMSE (m)	R^2
Dongdao Island	1.52	0.92
Yongxing Island	1.47	0.95
Yongle Atoll	1.69	0.89
Mean values	1.560	0.920

**Figure 7.** Scatter plots comparing estimated and measured water depths using the IPDB model: (a) Dongdao Island; (b) Yongxing Island; (c) Yongle Atoll.

5. Discussion

5.1. Advantages of the Improved Model

In the IPDB model, the estimation of the diffuse attenuation coefficient is a critical factor that determines the accuracy of depth retrieval. Thus, this study compares three methods for estimating the diffuse attenuation coefficient. While the P-DLA model uses the QAA, the proposed IPDB model introduces two variations of the SOA, each based on different sampling pixel sources. The evaluation results for each algorithm are detailed in Table 4.

Table 4 shows the significant differences in bathymetric accuracy between the three methods. The QAA outperforms the first SOA approach, which only uses deep water sampling pixels, in Yongxing Island. Its performance is comparable to the second SOA approach, which uses both deep and shallow water sampling pixels. However, in Dongdao Island and Yongle Atoll, the QAA significantly underperforms compared to both SOA methods. The QAA shows an average RMSE of 2.673 m and an average R^2 of 0.707, which is considerably worse than the SOAs. The second SOA, with an average RMSE of 1.560 m and R^2 of 0.920, performs particularly well, especially in diverse bathymetric environments. Except for its slightly lower performance at Yongle Atoll compared to the first SOA, it consistently delivers superior results across other study areas. This demonstrates that the second SOA not only adapts well to varying depth environments but also significantly enhances the accuracy of the IPDB model's depth estimation. Overall, the SOAs, particularly the method that incorporates both deep and shallow water sampling pixels, have markedly improved the bathymetric accuracy of the IPDB model.

Table 4. Comparison of bathymetric accuracy for different models.

Method for Estimating Diffuse Attenuation Coefficients	Study Area	Bathymetric Accuracy	
		RMSE (m)	R ²
QAA	Dongdao Island	2.53	0.79
	Yongxing Island	1.50	0.95
	Yongle Atoll	3.99	0.38
	Mean values	2.673	0.707
SOA (using sample pixels from deep water only)	Dongdao Island	1.72	0.90
	Yongxing Island	2.01	0.92
	Yongle Atoll	1.61	0.90
	Mean values	1.780	0.907
SOA (using sample pixels from deep water and shallow water)	Dongdao Island	1.52	0.92
	Yongxing Island	1.47	0.95
	Yongle Atoll	1.69	0.89
	Mean values	1.560	0.920

5.2. Impact of Different Sample Pixel Distributions on Model Performance

The collection of various sample types is crucial for accurately estimating model parameters. However, this process can be influenced by subjective human factors. In the same study area, different researchers may select sample points with varying spatial distributions, thereby affecting the stability of model parameter estimation. To minimize this impact, sample collection should adhere to the following principles:

- (1) Select adjacent pixel pairs in regions of remote sensing images where the boundaries between “light” and “dark” areas are clearly defined. Avoid selecting adjacent pixels within the same substrate type, particularly in areas with ambiguous boundaries. Additionally, ensure that adjacent pixel pairs are positioned at different distances from the waterline.
- (2) In preprocessed remote sensing images, the waterline is usually clearly visible. When sampling near the waterline, choose pixels from different substrate types to avoid collecting samples from a single substrate type. It is also important to refrain from sampling in areas with excessively high reflectance. After performing percentage truncation stretching on the remote sensing images, sampling should avoid areas with a concentration of “bright” pixels.
- (3) When collecting samples of different depths within the same substrate type, ensure that sandy pixels from various depths within the study area are included.
- (4) For selecting pixels in deep water areas, choose regions where the substrate is not visible, and avoid sampling in transitional zones between optical shallow and optical deep waters.

By adhering to these sample collection principles, we further explore the impact of different sample pixel distributions on the performance of the IPDB model. When the coefficient of determination (R^2) for regression equations based on sandy sampling pixels from shallow water exceeds 0.9, the estimated ratio of the diffuse attenuation coefficients for the blue and green bands typically shows minimal variation. Therefore, this study does not delve deeply into the effects of different sandy pixel distributions on model performance. Instead, we focus on analyzing the influence of three types of sampling pixels on the IPDB model’s performance: adjacent pixel pairs of different depths at the boundaries of different substrate types, pixels of typical substrate types near the waterline, and pixels of optically deep water adjacent to optically shallow water.

5.2.1. Impact of Different Pixel Pair Distributions on Model Performance

Collecting adjacent pixel pairs is a critical step in estimating the optimal band rotation coefficient vector. Understanding how the spatial distribution of these pixel pairs affects

the performance of the IPDB model is essential. To investigate this, we re-collected two sets of adjacent pixel pairs with distinct spatial distributions, as illustrated in Figure 8. In this figure, Cases I, II, and III represent adjacent pixel pairs with completely different spatial distributions, with Case I aligned with the pixel pair distribution shown in Figure 4. The spatial distribution of pixels with the same substrate type but different depths, those typical of the substrate type near the waterline, and the optical deep water pixels adjacent to the optical shallow water are consistent with Figure 4.

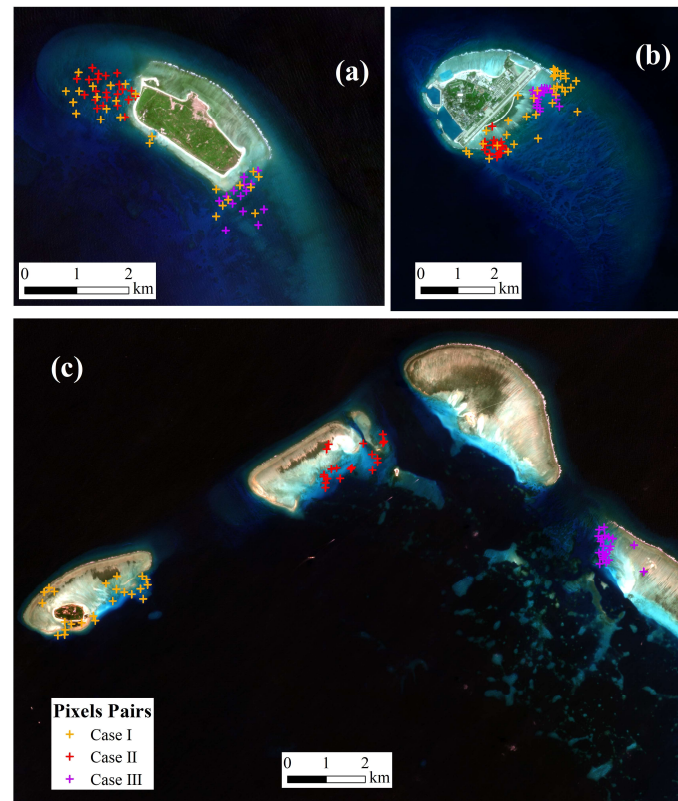


Figure 8. Distribution of different pixels pairs: (a) Dongdao Island; (b) Yongxing Island; (c) Yongle Atoll.

Table 5 presents the depth inversion results of the IPDB model under the three different spatial distributions of adjacent pixel pairs. By analyzing the RMSE and R^2 values across different study areas, it becomes evident that the performance of the IPDB model remains highly stable regardless of changes in the spatial distribution of adjacent pixel pairs. In Dongdao Island, the RMSE fluctuates only between 1.52 m and 1.54 m, while the R^2 consistently remains at 0.92. This indicates that the depth inversion results in this area are minimally influenced by the spatial distribution of adjacent pixel pairs, showcasing the model's robustness. Similarly, the performance of the IPDB model on Yongxing Island is notably stable. The RMSE varies from 1.45 m to 1.50 m, with R^2 values ranging from 0.95 to 0.96. Particularly under Case III, the R^2 reaches 0.96, reflecting outstanding performance in this area. For Yongle Atoll, despite the more complex environmental conditions, the IPDB model still demonstrates good stability. The RMSE ranges from 1.46 m to 1.69 m, with R^2 values between 0.89 and 0.92. Although the RMSE is slightly higher compared to the other two study areas, the overall performance of the model remains robust.

Table 5. Depth inversion results of the IPDB model based on different adjacent pixel pair distributions.

Study Area	Case	RMSE (m)	R^2
Dongdao Island	I	1.52	0.92
	II	1.53	0.92
	III	1.54	0.92
	Mean	1.530	0.920
Yongxing Island	I	1.47	0.95
	II	1.50	0.95
	III	1.45	0.96
	Mean	1.473	0.953
Yongle Atoll	I	1.69	0.89
	II	1.46	0.92
	III	1.51	0.91
	Mean	1.553	0.907

In summary, the depth inversion results of the IPDB model under different spatial distributions of adjacent pixel pairs are remarkably similar. The average RMSE and average R^2 values across the study areas further illustrate the robustness of the model. Specifically, the average RMSE for Dongdao Island is 1.530 m, with an average R^2 of 0.920; for Yongxing Island, the average RMSE is 1.473 m, and the average R^2 is 0.953; while Yongle Atoll shows an average RMSE of 1.553 m and an average R^2 of 0.907. These results indicate that the IPDB model maintains high accuracy despite variations in the spatial distribution of adjacent pixel pairs, demonstrating its strong applicability.

5.2.2. Impact of Different Waterline Distributions on Model Performance

Collecting waterline pixels is a crucial step in calculating bottom parameters, making it important to examine how the spatial distribution of these sampled pixels affects the performance of the IPDB model. To this end, we re-collected two sets of waterline sampling pixels with different spatial distributions, as shown in Figure 9. In this figure, Cases I, II, and III exhibit completely different spatial distributions of waterline sampling pixels, with Case I aligning with the distribution of waterline sampling pixels presented in Figure 4. The spatial distribution of adjacent pixel pairs at varying depths along different substrate type boundaries, pixels of the same substrate type but at different depths, and optical deep water pixels adjacent to optical shallow water remains consistent with Figure 4.

Table 6 presents the depth inversion results of the IPDB model based on different distributions of waterline sampling pixels. It is evident that, despite the variations in the spatial distribution of waterline pixels across different study areas, the model consistently demonstrates stability in performance. In Dongdao Island, although the distribution of waterlines varies significantly, the model's performance remains closely aligned across all cases, with RMSE fluctuating by only 0.06 m and R^2 varying by just 0.01. This indicates that the impact of different waterline distributions on parameter estimation is minimal. Similarly, in Yongxing Island, the RMSE and R^2 values show almost no significant differences across the three waterline distributions, particularly in Case III, where the RMSE is lowest and R^2 is highest. This finding suggests that even with changes in waterline pixel distribution, the model maintains a high level of inversion accuracy in this area, reflecting its robustness and adaptability. For Yongle Atoll, despite having higher RMSE values, the model performance remains relatively stable. The RMSE ranges from 1.62 m to 1.69 m, while R^2 values range between 0.89 and 0.90, with minimal fluctuations. This stability indicates that the spatial distribution of waterline sampling pixels has a limited effect on model performance.

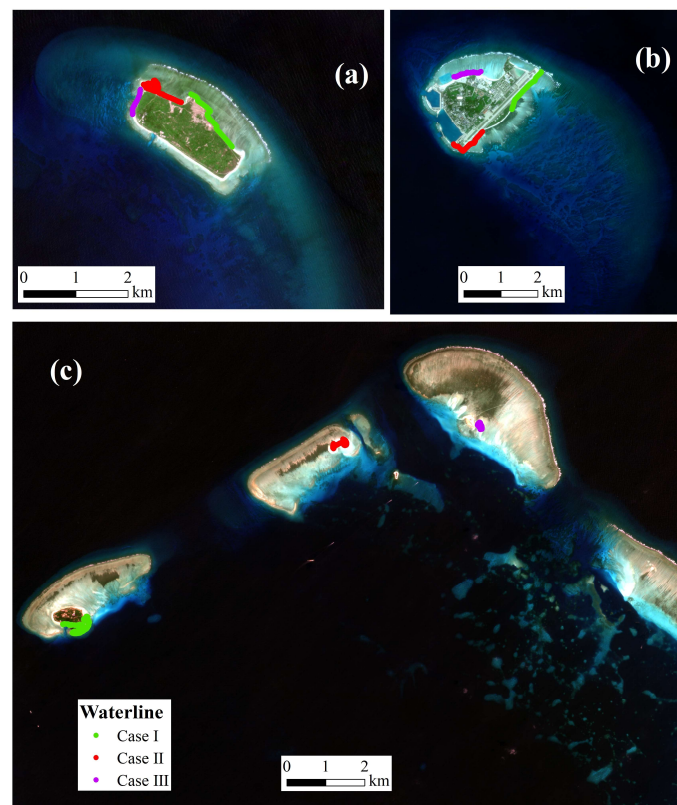


Figure 9. Distribution of different waterlines: (a) Dongdao Island; (b) Yongxing Island; (c) Yongle Atoll.

Table 6. Depth inversion results of the IPDB model based on different waterline sampling pixel distributions.

Study Area	Case	RMSE (m)	R^2
Dongdao Island	I	1.52	0.92
	II	1.46	0.93
	III	1.48	0.93
	Mean	1.487	0.927
Yongxing Island	I	1.47	0.95
	II	1.50	0.95
	III	1.44	0.96
	Mean	1.470	0.953
Yongle Atoll	I	1.69	0.89
	II	1.62	0.90
	III	1.66	0.89
	Mean	1.657	0.893

In summary, across Dongdao Island, Yongxing Island, and Yongle Atoll, the influence of different waterline distributions on the model's performance is minor. The IPDB model is capable of maintaining consistent inversion accuracy under various sampling conditions, demonstrating its adaptability and stability in diverse and complex environments.

5.2.3. Impact of Different Deep Water Distributions on Model Performance

Sampling pixels from deep water regions is a critical step in estimating the diffuse attenuation coefficients for the blue and green bands. It is important to explore how the spatial distribution of these deep water sampling pixels affects the performance of the

IPDB model. To this end, we re-collected three sets of deep water sampling pixels with different spatial distributions, as shown in Figure 10. In this figure, the sampling pixels at the waterline in Cases I, II, III, and IV exhibit completely different spatial distributions, with Case I aligning with the distribution of waterline sampling pixels depicted in Figure 4. The spatial distributions of adjacent pixels at different depths along the boundaries of various substrate types, as well as pixels of the same substrate type at different depths and typical substrate type pixels near the waterline, all correspond to those shown in Figure 4.

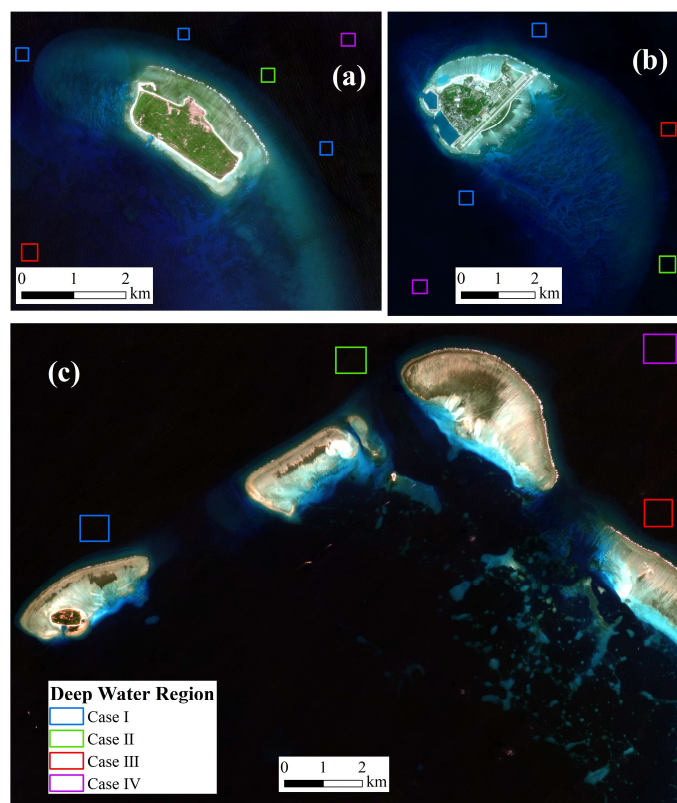


Figure 10. Distribution of different deep water regions: (a) Dongdao Island; (b) Yongxing Island; (c) Yongle Atoll.

Table 7 presents the results of the IPDB model's depth estimation based on different deep water pixel distributions. Despite the variability in the spatial distribution of deep water sampling pixels, the IPDB model demonstrates consistent stability. For instance, in Dongdao Island, the R^2 values for Cases I, II, III, and IV remain consistently at 0.92, indicating that the differences in deep water pixel distribution have minimal impact on the model's fitting performance. However, the RMSE values show slight fluctuations ranging from 1.50 m to 1.58 m, suggesting that the distribution of deep water sampling pixels does influence the model's depth estimation accuracy to some extent. Overall, the error variation is relatively minor, highlighting the model's stability.

Yongxing Island exhibits even better performance, with R^2 values exceeding 0.95 across all deep water distributions, peaking at 0.96. This reflects a high degree of model fit in this area, largely unaffected by the spatial distribution of deep water sampling pixels. The RMSE values also show minimal variation, ranging from 1.41 m to 1.47 m, indicating that the impact of different deep water distributions on model accuracy is extremely limited, underscoring the model's robustness.

In Yongle Atoll, although the RMSE values are slightly higher, the model performance remains stable across varying deep water distributions. The RMSE fluctuates between 1.62 m and 1.73 m, while R^2 values range from 0.88 to 0.90. This stability suggests that

despite the greater complexity of the deep water region in Yongle Atoll, the model maintains a relatively strong performance with limited variability in accuracy.

Table 7. Depth inversion results of the IPDB model based on different deep water pixel distributions.

Study Area	Case	RMSE (m)	R ²
Dongdao Island	I	1.52	0.92
	II	1.50	0.92
	III	1.55	0.92
	IV	1.58	0.92
	Mean	2.643	0.768
Yongxing Island	I	1.47	0.95
	II	1.42	0.96
	III	1.43	0.96
	IV	1.41	0.96
	Mean	1.433	0.958
Yongle Atoll	I	1.69	0.89
	II	1.73	0.88
	III	1.62	0.90
	IV	1.66	0.89
	Mean	1.675	0.890

Overall, the spatial distribution of deep water pixels has a limited impact on the performance of the IPDB model. This indicates that the IPDB model can adapt to various deep water distribution conditions while maintaining high accuracy and stability in depth estimations. Although some differences in RMSE exist across the study areas, the overall performance remains consistent, further affirming the robustness and reliability of the IPDB model in handling variations in deep water pixel distributions.

5.3. Comparison of Model Performance for Different Band Combinations

As shown in Equation (8), any two visible light bands can be used to construct a dual-band log-linear model, forming what is referred to as a band combination. The SuperDove imagery provides six visible light bands. To explore the impact of different band combinations on the performance of the IPDB model, this study selected two bands from the five most water-penetrating bands of SuperDove to construct the model's analytical expression. Additionally, these two bands were combined with the red band to estimate the parameters g_1 and g_2 using the Spectral Optimization Algorithm (SOA). The test area for this study was Yongle Atoll, and the specific band combinations considered were as follows: Combination I (coastal and green I bands), Combination II (coastal and green bands), Combination III (blue and green I bands), Combination IV (blue and green bands), Combination V (green I and green bands), Combination VI (coastal and yellow bands), and Combination VII (blue and yellow bands). The comparison results on the validation set are presented in Table 8.

Table 8. Model performance for different band combinations (Yongle Atoll).

Band Combination	RMSE (m)	R ²
I	3.25	0.59
II	2.99	0.65
III	1.99	0.85
IV	1.69	0.89
V	1.56	0.91
VI	2.67	0.72
VII	2.90	0.67

From Table 8, it is evident that band Combinations III (blue and green I), IV (blue and green), and V (green I and green) significantly outperform the other combinations in Yongle Atoll, with Combination V showing the best performance. To further identify a band combination with strong generalizability and optimal model performance, a comparative analysis of these three combinations (III to V) was conducted across Dongdao Island, Yongxing Island, and Yongle Atoll. The validation results are summarized in Table 9.

Table 9 compares the model performance of Combinations III, IV, and V across different water depth ranges in Dongdao Island, Yongxing Island, and Yongle Atoll. In Dongdao Island, the RMSE of Combination IV was 1.52 m, which was lower than that of Combination III (1.70 m) and Combination V (1.77 m), and had the best overall performance. In the 0–5 m depth range, Combinations IV (RMSE 1.47 m) and III (RMSE 1.62 m) performed well, while Combination V showed a slightly better RMSE of 1.38 m compared to Combination IV. As the depth increased, Combination IV excelled in the 5–15 m range with an RMSE of 1.16 m, indicating superior accuracy. In the 15–25 m range, although Combination IV (RMSE 2.58 m) performed slightly worse than Combination III (RMSE 2.52 m), it maintained better overall performance in Dongdao Island.

In Yongxing Island, Combination IV again led with an overall RMSE of 1.47 m, outperforming Combination III (RMSE 2.25 m) and Combination V (RMSE 1.97 m). In the 0–5 m range, Combination IV excelled with a remarkable RMSE of 0.89 m, clearly surpassing Combinations III (1.41 m) and V (0.93 m). Combinations IV maintained strong performance in the 5–15 m and 15–25 m ranges, demonstrating stability across various depths.

For Yongle Atoll, Combination V exhibited an overall RMSE of 1.56 m, which was better than Combination IV (RMSE 1.69 m) and Combination III (RMSE 1.99 m). In the 0–5 m and 5–15 m ranges, Combination V had RMSE values of 0.66 m and 1.36 m, respectively, showing good performance, although it faced greater fluctuations in the 15–25 m range (RMSE 5.21 m), indicating less reliability at deeper depths compared to Combination IV.

Table 9. Comparison of model performance for band Combinations III to V across three study areas.

Study Area	Band Combination	Water Depth Range (m)	RMSE (m)
Dongdao Island	III	Overall	1.70
		0–5	1.62
		5–15	1.48
		15–25	2.52
	IV	Overall	1.52
		0–5	1.47
		5–15	1.16
		15–25	2.58
	V	Overall	1.77
		0–5	1.38
		5–15	1.26
		15–25	3.61
Yongxing Island	III	Overall	2.25
		0–5	1.41
		5–15	2.11
		15–25	3.62
	IV	Overall	1.47
		0–5	0.89
		5–15	1.14
		15–25	2.51
	V	Overall	1.97
		0–5	0.93
		5–15	1.38
		15–25	3.76

Table 9. Cont.

Study Area	Band Combination	Water Depth Range (m)	RMSE (m)
Yongle Atoll	III	Overall	1.99
		0–5	1.46
		5–15	2.05
		15–25	4.74
	IV	Overall	1.69
		0–5	0.73
		5–15	1.32
		15–25	4.93
	V	Overall	1.56
		0–5	0.66
		5–15	1.36
		15–25	5.21
Mean Values	III	Overall	1.980
		0–5	1.497
		5–15	1.880
		15–25	3.627
	IV	Overall	1.560
		0–5	1.030
		5–15	1.207
		15–25	3.340
	V	Overall	1.767
		0–5	0.990
		5–15	1.333
		15–25	4.193

Overall, Combination IV (blue and green bands) is recommended as the optimal choice for constructing a physics-based dual-band model, while Combination V (green I and green bands) also shows promising results in shallow water areas.

6. Conclusions and Future Work

To address the issue of poor result stability in the P-DLA model caused by the QAA, and to evaluate the potential of SuperDove imagery for bathymetric estimation without prior depth data, this study developed an improved version of the P-DLA model, the IPDB model. This model replaces the QAA with a Spectral Optimization Algorithm (SOA) that integrates deep and shallow water pixels to estimate the diffuse attenuation coefficients for the blue and green bands, allowing for more accurate shallow water depth estimation. The IPDB model was applied to SuperDove imagery from Dongdao Island, Yongxing Island, and Yongle Atoll, yielding the following conclusions.

- (1) SuperDove imagery demonstrates the ability to estimate shallow water depth in the absence of prior depth data. The IPDB model applied to three study areas produced an RMSE of less than 1.7 m and an R^2 greater than 0.89, indicating strong bathymetric performance.
- (2) The P-DLA model with the QAA performs significantly worse than the IPDB model with the SOA. By incorporating both deep and shallow water pixels, the SOA significantly improves the accuracy of depth estimation.
- (3) Four sampling principles are summarized which, if followed, have no significant impact on model performance due to changes in the spatial distribution of sample pixels.
- (4) Among the five most water-penetrating bands in SuperDove images, the blue–green band combination is recommended as the optimal choice for constructing the analytical expression of the physics-based dual-band model.

Semi-analytical models, such as the IPDB, typically require high-quality imaging conditions. To mitigate the IPDB model's sensitivity to image quality, future studies may explore the possibility of stacking multiple high-resolution multispectral images to generate a single, clear, high-quality image. However, the IPDB model also has a notable limitation: it requires sufficiently long waterline features in the target area. This can be problematic in

certain coral reef regions, where such conditions may not always be met. Future research could focus on overcoming this limitation to enhance the model's broader applicability.

Author Contributions: Conceptualization, C.H. and Q.J.; methodology, C.H.; software, C.H.; validation, C.H., Q.J. and P.W.; formal analysis, C.H. and Q.J.; investigation, C.H.; resources, C.H.; data curation, C.H.; writing—original draft preparation, C.H.; writing—review and editing, C.H., Q.J. and P.W.; visualization, C.H.; supervision, C.H.; project administration, Q.J.; funding acquisition, Q.J. All authors have read and agreed to the published version of the manuscript.

Funding: This study was supported by the China Geological Survey Project (Project Number: DD20191011).

Data Availability Statement: The in situ bathymetric data used in this study are fully available at the National Earth System Science Data Center (<https://www.geodata.cn>, accessed on 3 July 2024). The remote sensing imagery is available from Planet Labs (www.planet.com/account, accessed on 28 June 2024) in the form of PlanetScope SuperDove Level 3B surface reflectance data products.

Acknowledgments: The authors would like to thank Planet Labs, Inc. for providing Super Dove satellite remote sensing data. Additionally, the authors would like to thank the National Earth System Science Data Center for providing the in situ bathymetric data.

Conflicts of Interest: The authors declare no conflicts of interest.

References

1. Ashphaq, M.; Srivastava, P.K.; Mitra, D. Review of near-shore satellite derived bathymetry: Classification and account of five decades of coastal bathymetry research. *J. Ocean Eng. Sci.* **2021**, *6*, 340–359. [CrossRef]
2. Pacheco, A.; Horta, J.; Loureiro, C.; Ferreira, Ó. Retrieval of nearshore bathymetry from Landsat 8 images: A tool for coastal monitoring in shallow waters. *Remote Sens. Environ.* **2015**, *159*, 102–116. [CrossRef]
3. Kerr, J.M.; Purkis, S. An algorithm for optically-deriving water depth from multispectral imagery in coral reef landscapes in the absence of ground-truth data. *Remote Sens. Environ.* **2018**, *210*, 307–324. [CrossRef]
4. Liu, Y.; Zhao, J.; Deng, R.; Liang, Y.; Gao, Y.; Chen, Q.; Xiong, L.; Liu, Y.; Tang, Y.; Tang, D. A downscaled bathymetric mapping approach combining multitemporal Landsat-8 and high spatial resolution imagery: Demonstrations from clear to turbid waters. *ISPRS J. Photogramm. Remote Sens.* **2021**, *180*, 65–81. [CrossRef]
5. Ma, S.; Tao, Z.; Yang, X.; Yu, Y.; Zhou, X.; Li, Z. Bathymetry Retrieval from Hyperspectral Remote Sensing Data in Optical-Shallow Water. *IEEE Trans. Geosci. Remote Sens.* **2014**, *52*, 1205–1212. [CrossRef]
6. Huang, Y.; Yang, H.; Tang, S.; Liu, Y.; Liu, Y. An Appraisal of Atmospheric Correction and Inversion Algorithms for Mapping High-Resolution Bathymetry over Coral Reef Waters. *IEEE Trans. Geosci. Remote Sens.* **2023**, *61*, 1–11. [CrossRef]
7. Peng, K.; Xie, H.; Xu, Q.; Huang, P.; Liu, Z. A Physics-Assisted Convolutional Neural Network for Bathymetric Mapping Using ICESat-2 and Sentinel-2 Data. *IEEE Trans. Geosci. Remote Sens.* **2022**, *60*, 1–13. [CrossRef]
8. Cahalane, C.; Magee, A.; Monteys, X.; Casal, G.; Hanafin, J.; Harris, P. A comparison of Landsat 8, RapidEye and Pleiades products for improving empirical predictions of satellite-derived bathymetry. *Remote Sens. Environ.* **2019**, *233*, 111414. [CrossRef]
9. Chen, A.; Ma, Y.; Zhang, J. Partition satellite derived bathymetry for coral reefs based on spatial residual information. *Int. J. Remote Sens.* **2021**, *42*, 2807–2826. [CrossRef]
10. McCarthy, M.J.; Otis, D.B.; Hughes, D.; Muller-Karger, F.E. Automated high-resolution satellite-derived coastal bathymetry mapping. *Int. J. Appl. Earth Obs. Geoinf.* **2022**, *107*, 102693. [CrossRef]
11. Shen, W.; Chen, M.; Wu, Z.; Wang, J. Shallow-Water Bathymetry Retrieval Based on an Improved Deep Learning Method Using GF-6 Multispectral Imagery in Nanshan Port Waters. *IEEE J. Sel. Top. Appl. Earth Obs. Remote Sens.* **2023**, *16*, 8550–8562. [CrossRef]
12. Ji, X.; Ma, Y.; Zhang, J.; Xu, W.; Wang, Y. A Sub-Bottom Type Adaption-Based Empirical Approach for Coastal Bathymetry Mapping Using Multispectral Satellite Imagery. *Remote Sens.* **2023**, *15*, 3570. [CrossRef]
13. Chu, S.; Cheng, L.; Cheng, J.; Zhang, X.; Zhang, J.; Chen, J.; Liu, J. Shallow water bathymetry based on a back propagation neural network and ensemble learning using multispectral satellite imagery. *Acta Oceanol. Sin.* **2023**, *42*, 154–165. [CrossRef]
14. Li, N.; Tang, Q.; Chen, Y.; Dong, Z.; Li, J.; Fu, X. Satellite-derived bathymetry integrating spatial and spectral information of multispectral images. *Appl. Opt.* **2023**, *62*, 2017–2029. [CrossRef]
15. Gupta, G.K.; Bhat, R.V.; Balan, M.S. Improving Satellite-Derived Bathymetry Estimation with a Joint Classification–Regression Model. *IEEE Geosci. Remote Sens. Lett.* **2024**, *21*, 1–5. [CrossRef]
16. Han, T.; Zhang, H.; Cao, W.; Le, C.; Wang, C.; Yang, X.; Ma, Y.; Li, D.; Wang, J.; Lou, X. Cost-efficient bathymetric mapping method based on massive active–passive remote sensing data. *ISPRS J. Photogramm. Remote Sens.* **2023**, *203*, 285–300. [CrossRef]
17. Ma, Y.; Xu, N.; Liu, Z.; Yang, B.; Yang, F.; Wang, X.H.; Li, S. Satellite-derived bathymetry using the ICESat-2 lidar and Sentinel-2 imagery datasets. *Remote Sens. Environ.* **2020**, *250*, 112047. [CrossRef]

18. Zhong, J.; Sun, J.; Lai, Z. ICESat-2 and Multispectral Images Based Coral Reefs Geomorphic Zone Mapping Using a Deep Learning Approach. *IEEE J. Sel. Top. Appl. Earth Obs. Remote Sens.* **2024**, *17*, 6085–6098. [[CrossRef](#)]
19. Hsu, H.-J.; Huang, C.-Y.; Jasinski, M.; Li, Y.; Gao, H.; Yamanokuchi, T.; Wang, C.-G.; Chang, T.-M.; Ren, H.; Kuo, C.-Y.; et al. A semi-empirical scheme for bathymetric mapping in shallow water by ICESat-2 and Sentinel-2: A case study in the South China Sea. *ISPRS J. Photogramm. Remote Sens.* **2021**, *178*, 1–19. [[CrossRef](#)]
20. Le, Y.; Hu, M.; Chen, Y.; Yan, Q.; Zhang, D.; Li, S.; Zhang, X.; Wang, L. Investigating the Shallow-Water Bathymetric Capability of Zhuhai-1 Spaceborne Hyperspectral Images Based on ICESat-2 Data and Empirical Approaches: A Case Study in the South China Sea. *Remote Sens.* **2022**, *14*, 3406. [[CrossRef](#)]
21. Liu, Y.; Zhou, Y.; Yang, X. Bathymetry derivation and slope-assisted benthic mapping using optical satellite imagery in combination with ICESat-2. *Int. J. Appl. Earth Obs. Geoinf.* **2024**, *127*, 103700. [[CrossRef](#)]
22. Zhang, X.; Ma, Y.; Li, Z.; Zhang, J. Satellite derived bathymetry based on ICESat-2 diffuse attenuation signal without prior information. *Int. J. Appl. Earth Obs. Geoinf.* **2022**, *113*, 102993. [[CrossRef](#)]
23. Wu, Z.; Tao, B.; Mao, Z.; Huang, H. Bathymetry Retrieval Algorithm Based on Hyperspectral Features of Pure Water Absorption From 570 to 600 nm. *IEEE Trans. Geosci. Remote Sens.* **2023**, *61*, 1–19. [[CrossRef](#)]
24. Huang, W.; Zhao, J.; Ai, B.; Sun, S.; Yan, N. Bathymetry and Benthic Habitat Mapping in Shallow Waters from Sentinel-2A Imagery: A Case Study in Xisha Islands, China. *IEEE Trans. Geosci. Remote Sens.* **2022**, *60*, 1–12. [[CrossRef](#)]
25. Liu, Y.; Deng, R.; Li, J.; Qin, Y.; Xiong, L.; Chen, Q.; Liu, X. Multispectral Bathymetry via Linear Unmixing of the Benthic Reflectance. *IEEE J. Sel. Top. Appl. Earth Obs. Remote Sens.* **2018**, *11*, 4349–4363. [[CrossRef](#)]
26. Liu, Y.; Deng, R.; Qin, Y.; Cao, B.; Liang, Y.; Liu, Y.; Tian, J.; Wang, S. Rapid estimation of bathymetry from multispectral imagery without in situ bathymetry data. *Appl. Opt.* **2019**, *58*, 7538–7551. [[CrossRef](#)]
27. Xia, H.; Li, X.; Zhang, H.; Wang, J.; Lou, X.; Fan, K.; Shi, A.; Li, D. A Bathymetry Mapping Approach Combining Log-Ratio and Semianalytical Models Using Four-Band Multispectral Imagery without Ground Data. *IEEE Trans. Geosci. Remote Sens.* **2020**, *58*, 2695–2709. [[CrossRef](#)]
28. Lee, Z.; Carder, K.L.; Mobley, C.D.; Steward, R.G.; Patch, J.S. Hyperspectral remote sensing for shallow waters: 2. Deriving bottom depths and water properties by optimization. *Appl. Opt.* **1999**, *38*, 3831–3843. [[CrossRef](#)]
29. Liu, Z. Bathymetry and bottom albedo retrieval using Hyperion: A case study of Thitu Island and reef. *Chin. J. Oceanol. Limnol.* **2013**, *31*, 1350–1355. [[CrossRef](#)]
30. Chu, S.; Cheng, L.; Ruan, X.; Zhuang, Q.; Zhou, X.; Li, M.; Shi, Y. Technical Framework for Shallow-Water Bathymetry with High Reliability and No Missing Data Based on Time-Series Sentinel-2 Images. *IEEE Trans. Geosci. Remote Sens.* **2019**, *57*, 8745–8763. [[CrossRef](#)]
31. Li, J.; Knapp, D.E.; Schill, S.R.; Roelfsema, C.; Phinn, S.; Silman, M.; Mascaro, J.; Asner, G.P. Adaptive bathymetry estimation for shallow coastal waters using Planet Dove satellites. *Remote Sens. Environ.* **2019**, *232*, 111302. [[CrossRef](#)]
32. Xu, Y.; Cao, B.; Deng, R.; Cao, B.; Liu, H.; Li, J. Bathymetry over broad geographic areas using optical high-spatial-resolution satellite remote sensing without in-situ data. *Int. J. Appl. Earth Obs. Geoinf.* **2023**, *119*, 103308. [[CrossRef](#)]
33. Huang, R.; Yu, K.; Wang, Y.; Wang, J.; Mu, L.; Wang, W. Bathymetry of the Coral Reefs of Weizhou Island Based on Multispectral Satellite Images. *Remote Sens.* **2017**, *9*, 750. [[CrossRef](#)]
34. Cao, B.; Liu, H.; Cao, B. Making satellite-derived empirical bathymetry independent of high-quality in-situ depth data: An assessment of four possible model calibration data. *ISPRS J. Photogramm. Remote Sens.* **2024**, *211*, 336–355. [[CrossRef](#)]
35. Chen, B.; Yang, Y.; Xu, D.; Huang, E. A dual band algorithm for shallow water depth retrieval from high spatial resolution imagery with no ground truth. *ISPRS J. Photogramm. Remote Sens.* **2019**, *151*, 1–13. [[CrossRef](#)]
36. Zhu, W.; Ye, L.; Qiu, Z.; Luan, K.; He, N.; Wei, Z.; Yang, F.; Yue, Z.; Zhao, S.; Yang, F. Research of the Dual-Band Log-Linear Analysis Model Based on Physics for Bathymetry without In-Situ Depth Data in the South China Sea. *Remote Sens.* **2021**, *13*, 4331. [[CrossRef](#)]
37. Yang, Q.; Chen, J.; Chen, B.; Tao, B. Evaluation and Improvement of No-Ground-Truth Dual Band Algorithm for Shallow Water Depth Retrieval: A Case Study of a Coastal Island. *Remote Sens.* **2022**, *14*, 6231. [[CrossRef](#)]
38. Hedley, J.D.; Harborne, A.R.; Mumby, P.J. Technical note: Simple and robust removal of sun glint for mapping shallow-water benthos. *Int. J. Remote Sens.* **2007**, *26*, 2107–2112. [[CrossRef](#)]
39. Philpot, W.D. Bathymetric mapping with passive multispectral imagery. *Appl. Opt.* **1988**, *28*, 1569–1578. [[CrossRef](#)]
40. Wei, J.; Wang, M.; Lee, Z.; Briceño, H.O.; Yu, X.; Jiang, L.; Garcia, R.; Wang, J.; Luis, K. Shallow water bathymetry with multispectral satellite ocean color sensors: Leveraging temporal variation in image data. *Remote Sens. Environ.* **2020**, *250*, 112035. [[CrossRef](#)]
41. Lee, Z.; Carder, K.L.; Mobley, C.D.; Steward, R.G.; Patch, J.S. Hyperspectral remote sensing for shallow waters. I. A semianalytical model. *Appl. Opt.* **1998**, *37*, 6329–6338. [[CrossRef](#)] [[PubMed](#)]
42. Zhang, X.; Ma, Y.; Zhang, J. Shallow Water Bathymetry Based on Inherent Optical Properties Using High Spatial Resolution Multispectral Imagery. *Remote Sens.* **2020**, *12*, 3027. [[CrossRef](#)]

43. Zhan, J.; Zhang, D.; Tan, L.; Zhang, G.; Župan, R. Performance analysis of inverting optical properties based on quasi-analytical algorithms. *Multimed. Tools Appl.* **2021**, *81*, 4693–4709. [[CrossRef](#)]
44. Van der Linden, S.; Rabe, A.; Held, M.; Jakimow, B.; Leitão, P.; Okujeni, A.; Schwieder, M.; Suess, S.; Hostert, P. The EnMAP-Box—A Toolbox and Application Programming Interface for EnMAP Data Processing. *Remote Sens.* **2015**, *7*, 11249–11266. [[CrossRef](#)]

Disclaimer/Publisher’s Note: The statements, opinions and data contained in all publications are solely those of the individual author(s) and contributor(s) and not of MDPI and/or the editor(s). MDPI and/or the editor(s) disclaim responsibility for any injury to people or property resulting from any ideas, methods, instructions or products referred to in the content.